

Binomial Self-Compensation: Mechanism and Suppression of Motion Error in Phase-Shifting Profilometry

Geyou Zhang, Kai Liu, *Senior Member, IEEE*, and Ce Zhu*, *Fellow, IEEE*

Abstract—Phase shifting profilometry (PSP) is widely used in high-precision 3D scanning due to its high accuracy, robustness, and pixel-wise handling. However, a fundamental assumption of PSP that the object should remain static does not hold in dynamic measurement, making PSP susceptible to object motion. To address this challenge, our proposed solution, phase-sequential binomial self-compensation (P-BSC), sums successive motion-affected phase frames weighted by binomial coefficients. This approach exponentially reduces the motion error in a pixel-wise and frame-wise loopable manner. Despite its efficacy, P-BSC suffers from high computational overhead and error accumulation due to its reliance on multi-frame phase calculations and weighted summations. Inspired by P-BSC, we propose an image-sequential binomial self-compensation (I-BSC) to weight sum the homogeneous fringe images instead of successive phase frames, which generalizes the BSC concept from phase sequences to image sequences. I-BSC computes the arctangent function only once, resolving both limitations in P-BSC. Extensive analysis, simulations, and experiments show that 1) the proposed BSC outperforms existing methods in reducing motion error while achieving a quasi-single-shot frame rate, i.e., depth map frame rate equals to the camera's acquisition rate, enabling 3D reconstruction with high pixel-depth-temporal resolution; 2) compared to P-BSC, our I-BSC reduces the computational complexity by one polynomial order, thereby accelerating the computational frame rate by several to dozen times, while also reaching faster motion error convergence.

Index Terms—Phase shifting profilometry, dynamic 3D scanning, binomial self-compensation, motion error, stereo phase unwrapping.

I. INTRODUCTION

In recent years, structured light (SL) 3D imaging has been penetrated into diverse fields, e.g., industrial inspection [1] and design [2], medical 3D reconstruction [3], [4], virtual reality [5], and digitalization of cultural heritage [6]. Phase shifting profilometry (PSP) [7], Fourier transform profilometry, and Gray code [8] are famous SL technologies that are widely applied in industry and scientific research. Among the SL technologies above, PSP is especially favored in high-precision 3D scanning due to its high accuracy, robustness, and pixel-wise property [9]. Many studies have excavated the huge potentiality of PSP in various challenging scenes [10], such as low signal-to-noise [11], [12], multi-path [13]–[15], high reflectivity [16], asynchronous shooting [17], and global illumination [18]–[21], etc.

This work was supported by the National Natural Science Foundation of China under Grant No. 62020106011.

G. Zhang and C. Zhu are with the School of Information and Communication Engineering, University of Electronic Science and Technology of China, Chengdu, China, 611731.

K. Liu is with College of Electrical Engineering, Sichuan University, Chengdu, China, 610065.

Corresponding author: C. Zhu, Email: eczhu@uestc.edu.cn.

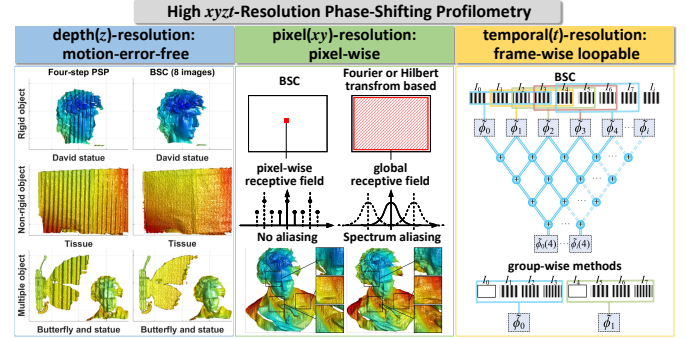


Fig. 1. Left: BSC substantially reduces the ripple-like motion error in traditional four-step PSP; Middle: BSC operates independently for each pixel, unlike existing methods based on Fourier transform, Hilbert transform, or convolution, which rely on global or neighborhood image information; Right: BSC achieves a depth map frame rate consistent with the image acquisition frame rate due to its frame-wise loopable nature.

However, a fundamental assumption of PSP that the object should remain static is violated in dynamic measurement, making PSP susceptible to object moving, resulting in ripple-like errors in the point clouds. Despite numerous researchers have explored fringe projection [22]–[24] and unwrapping strategies [25]–[30] using fewer patterns [31], [32], the motion error remains due to the multiple frame nature of PSP. In order to accomplish high-accuracy 3D reconstruction in dynamic scenes, the primarily challenge is **the motion-induced phase errors**, which urgently requires error correction algorithms [33]–[38], [38], [39], [39]–[43] to eliminate it.

Traditional PSP extracts phase information from fringe images using an arctangent function. This process involves only two types of variables: fringe images and phase. However, existing motion error compensation methods typically estimate or generate intermediate variables, which are then used—either directly or indirectly—to compute the motion-error-free phase, thereby complicating the phase retrieval process. For example, in phase shifting estimation methods, the intermediate variables are motion-induced phase shifting values [34]–[37], [44]; in object tracking methods, the intermediate variable is the rigid transform matrix [38]–[40]; in automatic compensation methods, the intermediate variables are the captured images after undergoing Hilbert transform [41] or differential operator [42]. The adoption of intermediate variables not only complicates the algorithm and degrades the real-time performance of calculations but also undermines the pixel-wise advantage of PSP. Therefore, a question naturally arises: **Why not use the motion-affected variables themselves to compensate for motion error, thus eschewing the occurrence of extra intermediate variables?**

To answer this question, without depending on any extra intermediate variable, our preliminary work, presented at the European Conference on Computer Vision 2024 [45], has initiated efforts to address the motion error issue by self-compensation. We develop a phase-sequential binomial self-compensation (**P-BSC**) method that only utilizes the motion-affected phase sequence itself, thereby effectively and flexibly eliminating the motion error. We cyclically [27] project high-frequency patterns with $\pi/2$ phase shifting, and directly compute a sequence of phase frames from each three or four successive captured images. By adding up a sequence of successive phase frames weighted by binomial coefficients, we achieve self-compensation of motion error. In summary, our P-BSC achieves high $xyzt$ resolution 3D scanning in dynamic scenes, specifically: **1) high depth resolution** (z -resolution): P-BSC can exponentially reduce the motion error as the binomial order K increases. **2) high pixel resolution** (xy -resolution): P-BSC inherits the pixel-wise advantages of PSP, which is independent for each pixel in an image, and thus obtains depth map of pixel-level granularity. **3) high temporal resolution** (t -resolution): P-BSC is of high temporal resolution to achieve quasi-single-shot 3D imaging frame rate due to its frame-wise loopable nature. It can be seen that P-BSC performs a linear combination on the phase sequence to suppress motion errors, thereby avoiding the generation of other types of intermediate variables.

Although P-BSC effectively suppresses motion errors, it faces two challenges: high computational overhead and error accumulation, arising from the need to calculate multi-frame phases and perform weighted summation. In this paper, inspired by the idea of weighted sum using binomial coefficients in the P-BSC, we propose a novel image-sequential binomial self-compensation (**I-BSC**) that only requires computing the arctangent function once. Our I-BSC fully inherits the high depth-pixel-temporal resolution of P-BSC, but the difference is, instead of summing up the **phase frames**, our I-BSC adds up the homogeneous **fringe images** weighted by the binomial coefficients, from which four compensated images are obtained to compute motion-error-free phase. Our theoretical analysis indicates that I-BSC can exponentially reduce the motion error, while reducing the time complexity of P-BSC by one polynomial order. Both simulations and experiments show that, compared to P-BSC, I-BSC accelerates the computational frame rate by several to dozen times, while also maintaining faster error convergence. This is attributed to the fact that I-BSC only needs to compute the arctangent function once, avoiding high computational overhead and error accumulation. It can be seen that I-BSC performs a linear combination on the image sequence to suppress motion errors, thereby avoiding the generation of other types of intermediate variables.

To address the phase unwrapping and nonlinearity issues that arise due to the limited number of patterns in dynamic scenes, on the one hand, we propose a paraxial stereo phase unwrapping (PSPU) method, thereby achieving unambiguous 3D point reconstruction using a single set of high-frequency fringe patterns. On the other hand, we propose a full-chain nonlinearity rectification (FNR) method in high-speed scenes, from which the nonlinear error in pattern illumination and

camera digitization that emerges due to the limited number of patterns is effectively suppressed.

Some preliminary results of this study were partially presented at the ECCV 2024¹. The contributions of this extended journal version are:

- We propose applying weighted summation to the successive phase frames using binomial coefficients, named phase-sequential binomial self-compensation (P-BSC), significantly reducing the motion error in PSP and achieving 3D scanning with high depth-pixel-temporal resolution.
- A novel image-sequential binomial self-compensation (I-BSC) algorithm is devised to address the high computational overhead and error accumulation issues of P-BSC, which generalizes the BSC concept from phase sequences to image sequences. Compared with P-BSC, I-BSC reduces computational complexity by one polynomial order, while reaching faster motion error convergence.
- A paraxial stereo phase unwrapping and full-chain rectification address the phase ambiguity and nonlinear issues that arise due to the limited number of patterns in dynamic scenes.
- We elaborate the error theory and computational complexity of both P-BSC and I-BSC from the perspectives of mechanism, simulation, and experimentation, providing comprehensive and detailed guidance for practical application.

Additionally, our P-BSC and I-BSC are simple yet effective, requiring no additional novel or customized patterns. Therefore, our method offers flexibility and ease of deployment, serving as an enhanced, motion-error-free version of the four-step PSP and providing a plug-and-play solution for dynamic 3D scanning scenarios. Various temporal and spatial phase unwrapping methods could benefit from our BSC strategy, resulting in fewer outliers and higher accuracy when faced with motion error.

II. RELATED WORK

With the rapid development of hardware measurement devices such as digital light processing (DLP) projector and high-speed camera, and the increasing demand for high-speed dynamic scene measurement, researchers are gradually shifting their attention from static scenes to dynamic scenes [6], e.g., structural dynamic measurement [46], stress-strain experiments on turbine blade [47], and vehicle crash

¹Compared with the conference version, this journal version is extended in the following aspects: 1) We extend the error model to N -step case and supplement the visual explanation of the P-BSC mechanism. 2) We reveal two issues arising from P-BSC's computation of multi-frame phases: high computational overhead and error accumulation. To address both issues, we propose a novel image-sequential binomial self-compensation method, which applies weighted summation to homogeneous fringe images instead of successive phase frames. 3) We improve our paraxial stereo unwrapping method to reduce outliers and propose a full-chain nonlinear correction scheme to alleviate the impact of nonlinearity on P-BSC and I-BSC performance. 4) The mechanisms, simulations, and experiments of P-BSC and I-BSC are significantly expanded to provide a comprehensive evaluation of their accuracy and computational efficiency. 5) We conduct simulations to demonstrate that our P-BSC and I-BSC are easy to deploy with popular temporal phase unwrapping methods, effectively reducing motion errors and outliers.

test [6]. PSP requires extra patterns to unwrap the high-frequency phase. Many studies have explored to reduce the number of needed patterns. Wang et al. [25] adopted a three-frequency heterodyne using 9 fringe patterns, from which they achieve a 3D measurement speed of 556 fps with a 5000 fps high-speed camera. Further, Zuo et al. [23] introduced a number-theoretical approach using a bi-frequency strategy to reconstruct the 3D point cloud with 5 fringe patterns. Gupta et al. [26] designed a micro phase shifting method to accomplish theoretically optimal in terms of the number of input images, which requires at least 4 fringe patterns in theory. As researchers continue to improve the encoding efficiency [28]–[30], Gray code is gradually employed on high-speed fringe projection measurement to assist phase unwrapping. Recently, Zhu et al. [24] designed (3 + 1) temporal overlapping Gray code pattern to achieve a superfast and large-depth-range 3D measurement.

Despite extensive efforts to reduce the number of patterns, motion error remains inevitable due to the multi-frame nature of PSP. Consequently, error compensation methods for high-speed scenarios have recently been developed. Based on specific implementation details, we categorize the motion error compensation methods into three classes: 1) motion-induced phase shifting estimation, 2) object tracking, and 3) automatic compensation.

Motion-induced phase shifting estimation: In traditional PSP, the phase shifting of each pattern is equally distributed or pre-known values within one period of fringe, which becomes disorderly due to object motion. Thus, researchers estimate the motion-induced phase shifting according to the implicit motion information in the motion-affected phase frame [33] or frames [34]–[37], [44], thereby restoring the unknown motion-affected phase shifting value of each pattern, and finally solve the corrected phase by least squared method. However, these methods may not effectively compensate for errors when the motion information can't be precisely predicted. **Object tracking:** By tracking the position of the object by placing markers [38] or using image feature matching algorithm [39], the motion error can be corrected by identifying the trajectory of the object [38]–[40]. However, a limitation of the object tracking based methods is that they are tailored for 2D motion perpendicular to the sight line. Moreover, the accuracy and reliability of feature tracking are crucial issues when faced with textureless or non-rigid objects. **Automatic compensation:** In automatic compensation methods, instead of computing motion-induced phase shifting value or tracking the object, an appropriate operator is selected to conduct on the whole captured image [41], [42] or phase frame [43], and further directly obtain the motion-error-free phase, in which the motion error will be automatically compensated.

From another perspective, we can also distinguish them based on their 3D reconstruction performance on pixel and temporal resolution. We examine the motion compensation methods from two perspectives: property of pixel-wise and frame-wise loopable. Pixel-wise methods compute phase and point clouds pixel by pixel, achieving spatial independence through this detailed granularity. Frame-wise loopable methods accomplish the same depth map frame rate as the camera

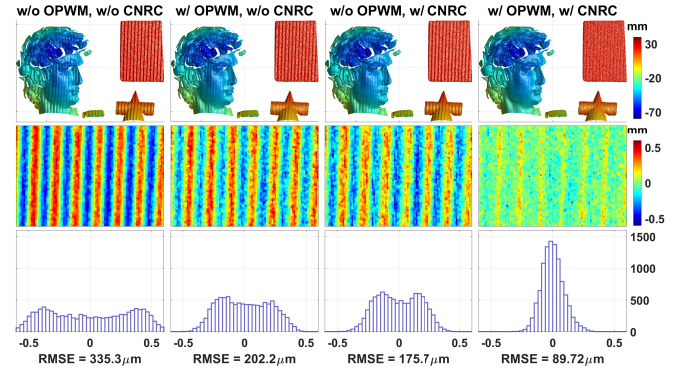


Fig. 2. OPWM and CNRC can effectively compensate nonlinearity in four-step PSP. Row 1: 3D reconstruction results of a scene of statue, geometry and plate; Row 2: error map of the plate in Row 1; Row 3: error histogram of the plate in Row 1.

acquisition frame rate, enabling a quasi-single-shot 3D reconstruction frame rate.

Pixel-wise: Several motion error compensation methods preserve the pixel-wise precision of traditional PSP, which utilizing two sampling phase frames to iteratively compute motion phase shifting [34], [37], automatically compensate for errors [43], tracking the position of the object by placing markers [38], using image feature matching algorithm [39] and correct motion error by identifying the trajectory of the object [38]–[40]. These approaches build on the granularity of pixel-level adjustments. In contrast, the non-pixel-wise methods conduct particular operator on local [33], [36], [42] or global image [35], [41], [48], e.g., Fourier transform [35], [44], [48], Hilbert transform [41], differential operator [42], mean filter [36], optimization algorithm [33], from which estimate the extra phase shifting induced by motion and compensate error [35], [36] or directly correct motion error [33], [41], [42], [48]. However, the pixel-wise merit of PSP is not preserved in these methods, theoretically diminishing their robustness in handling depth discontinuities. Concurrently, introducing extra non-pixel-wise operators also escalates the computational time required. **Frame-wise loopable:** By projecting high-frequency fringes and reconstructing 3D point clouds using a cyclic strategy [27], some motion error compensation methods [33], [36], [41]–[43] accomplish 3D reconstruction with quasi-single-shot frame rate, thus called frame-wise loopable methods in this paper. The cyclic strategy is not suitable for all motion compensation methods, some methods need to project an indivisible group of patterns [35], [37], [48], such that the depth map frame rate is reduced severalfold.

III. FULL-CHAIN NONLINEARITY RECTIFICATION

The nonlinear response inevitably exists in electronic and electrical systems. Specifically, in a structured light system, the nonlinear response occurs in pattern illumination and camera digitization. In static scenes, by increasing the number of patterns, the nonlinear harmonics can be significantly suppressed. However, in dynamic scenes, three- or four-step PSP is typically employed due to the real-time requirement, and thus the nonlinear error can't be overlooked. Moreover, the

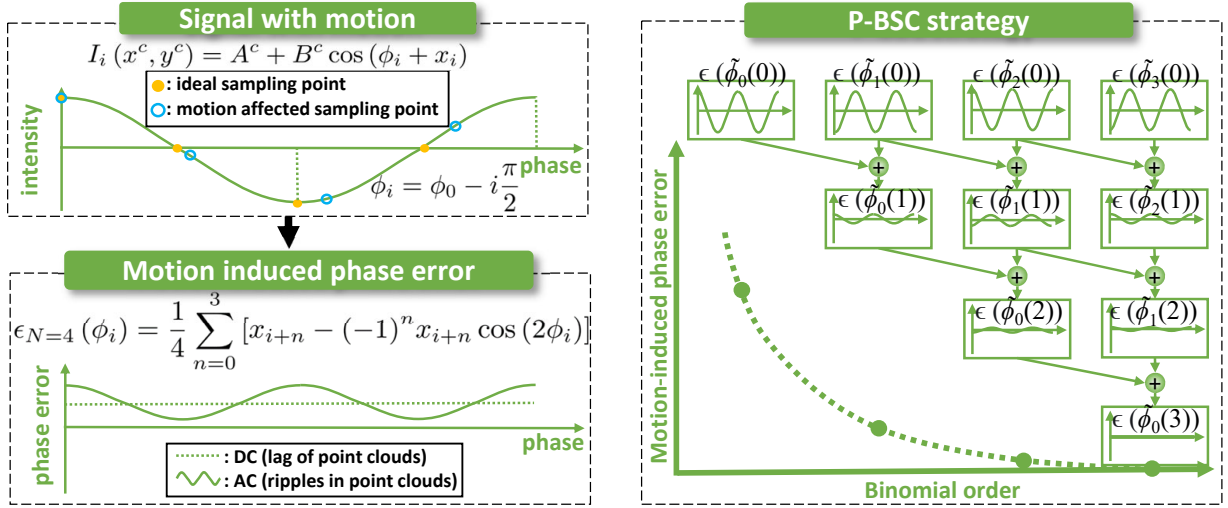


Fig. 3. Mechanism and characteristic of motion error, and how our solution, P-BSC, exponentially reduces the motion error by leveraging the its own characteristic.

nonlinear error can also compromises the performance of our algorithm, which will be elaborated in Section VI-B. In this section, we achieve a nonlinearity rectification in the full-chain for structured light imaging, providing assurance for accurate 3D imaging in high-speed scenes.

Optimal PWM Fringe Pattern: In high-speed 3D scanning, a DLP projector can achieve frame rates of tens of thousands when projecting binary patterns, yet it introduces higher-order harmonics. To mitigate the nonlinear response of projector radiant intensity to ideal pattern intensity, we employ optimal pulse width modulation (OPWM) [49] fringe pattern to eliminate specified order of harmonics that cause aliasing errors. **Camera Nonlinear Response:** The camera response function (CRF) is commonly recognized as a nonlinear single valued mapping, which compromises the linearity of sensor irradiance to image intensity. By employing DLP projector with high linearity achieved using digital mirror devices, we propose to synchronously capture multi-exposure images on a monochromatic scene illuminated by constant uniform light from the projector, which is named camera nonlinear response correction (CNRC). The implementation details can be found in the supplementary materials.

To demonstrate the performance of our FNC, we independently and jointly employ OPWM and CNRC to reconstruct a scene of statue, geometry and plate. The results shows that both OPWM and CNRC can effectively eliminating the ripple-like error induced by nonlinearity as shown in Fig. 2. Moreover, we obtain ripple-free point cloud if both OPWM and CNRC are conducted, achieving substantially nonlinearity rectification in the full-chain.

IV. BINOMIAL SELF-COMPENSATION FOR MOTION ERROR

A. Mechanism of Motion Error

The 3D point corresponding to a camera pixel \$(x^c, y^c)\$ is the intersection point of the sight line and the object surface. The intersection point moves along with the sight line on the circumstance that measures moving objects. Assuming the

object is of low-frequency texture, the \$i\$ th captured frame can be expressed as

$$I_i(x^c, y^c) = A + B \cos\left(\phi_0 - \frac{2\pi i}{N} + x_i\right), \quad (1)$$

where \$A\$ is the background intensity, \$B\$ is the modulation, \$x_i\$ represents the unknown phase offset induced by the motion from the datum frame to \$i\$-th frame, note that the datum frame can be arbitrarily chosen, and the true phase value at \$i\$ th frame is \$\phi_i = \phi_0 - \frac{2\pi i}{N}\$. The object motion causes the sampling point deviates from its ideal position as shown in Fig. 3.

The motion-affected phase can be typically calculated as

$$\tilde{\phi}_i = \tan^{-1} \left[\frac{\sum_{n=0}^{N-1} I_{i+n} \sin\left(\frac{2\pi n}{N}\right)}{\sum_{n=0}^{N-1} I_{i+n} \cos\left(\frac{2\pi n}{N}\right)} \right]. \quad (2)$$

We substitute Eq. (1) into Eq. (2) to evaluate the motion error, for a small phase-shift error \$x_i\$, \$\sin(x_i) \approx x_i\$ and \$\cos(x_i) \approx 1\$. Thus we have

$$\begin{aligned} \epsilon(\tilde{\phi}_i) &= \tilde{\phi}_i - \phi_i \\ &\approx \tan^{-1} \left[\frac{1}{N} \sum_{n=0}^{N-1} x_{i+n} (1 - \cos(2\phi_{i+n})) \right] \\ &\approx \frac{1}{N} \sum_{n=0}^{N-1} x_{i+n} (1 - \cos(2\phi_{i+n})) \end{aligned} \quad (3)$$

According to Eq. (3), as depicted in Fig. 3, the motion error comprises a DC component and a harmonic component with twice the frequency of the wrapped phase. The DC component, manifesting as the lag of the point clouds due to object motion, is independent of the phase value, and thus is irrelevant to the ripple-shaped error. Consequently, the crux of motion error compensation lies in eliminating the harmonic.

Further, we notice that Eq. (3) is complex due to the irregular trigonometric terms caused by \$2\pi/N\$-phase-shifting,

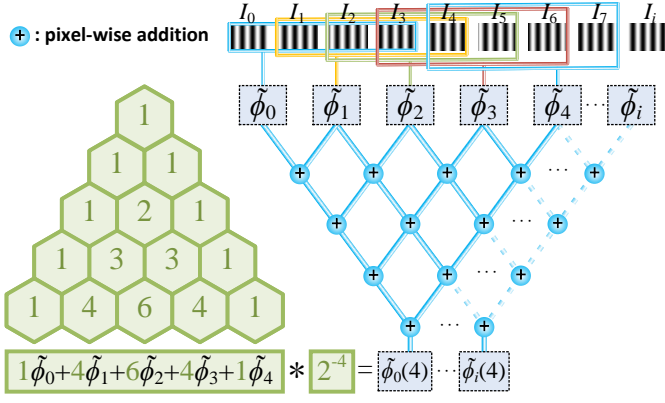


Fig. 4. Diagram of P-BSC.

except for the case when $N = 4$. When a $\pi/2$ -phase-shifting is adopted, the sign of the cosine term oscillates with the change of i without inducing any extra trigonometric term. Thus, the motion error is

$$\epsilon_{N=4}(\tilde{\phi}_i) = \frac{1}{4} \sum_{n=0}^3 [x_{i+n} - (-1)^n x_{i+n} \cos(2\phi_i)]. \quad (4)$$

B. Phase-sequential Binomial Self-Compensation

In this paper, by utilizing the proposed PSPU (will be illustrated in Section V), we achieve unambiguous 3D reconstruction within the specified depth range, using only a single set of high-frequency fringe patterns. Therefore, we adopt a cyclical N -step phase-shifting strategy [27] to project a group of high-frequency fringe patterns.

Analyzing the motion error waveform of two successive phase frames $\tilde{\phi}_i$ and $\tilde{\phi}_{i+1}$ in a discrete time series, we discover that the coefficients of trigonometric terms exhibit opposite signs owing to a phase shift of $\pi/2$ as shown in Fig. 3. Consequently, summing each pair of successive phase frames yields higher-order difference terms in the coefficients of harmonics. Repeating this process with the resultant phase frames, as depicted in Fig. 4, naturally evokes the concept of Yang Hui's triangle.

Let's consider calculating the weighted sum of $K + 1$ successive phase frames in a time series as shown in Fig. 4, using the $(K + 1)$ -th row of Yang Hui's triangle as the coefficients, also as known as K -th order binomial coefficients

$$\tilde{\phi}_i(K) = 2^{-K} \sum_{k=0}^K \binom{K}{k} \tilde{\phi}_{i+K-k}(0), \quad (5)$$

where $\tilde{\phi}_i(0)$ is computed by Eq. (2). Without loss of generality, we substitute Eq. (3) into Eq. (5) to have

$$\begin{aligned} \tilde{\phi}_i(K) = & 2^{-K} \sum_{k=0}^K \binom{K}{k} \left(\phi_{i+k} + \frac{1}{N} \sum_{n=0}^{N-1} x_{i+k+n} \right) \\ & - \frac{2^{-K}}{N} \sum_{k=0}^K \sum_{n=0}^{N-1} \binom{K}{k} x_{i+k+n} \cos(2\phi_{i+k+n}) \end{aligned} \quad (6)$$

the former term induces latency in point clouds which hardly compromises the absolute accuracy, while the later term causes ripple-like motion error.

We notice that x_i and its high order difference exactly correspond to the concepts of displacement, velocity, and acceleration, et. al, in kinematics, and can be expressed as

$$\begin{cases} \Delta^{(K)} x_i = \Delta^{(K-1)} x_{i+1} - \Delta^{(K-1)} x_i \\ \Delta^{(K)} x_i = \sum_{k=0}^K (-1)^k \binom{K}{k} x_{i+K-k} \end{cases}, \quad (7)$$

where we define $\Delta^{(0)} x_i = x_i$.

In the four-step PSP case, by putting Eq. (7) into Eq. (6), we can simply derive

$$\begin{aligned} \tilde{\phi}_i^4(K) &= \bar{\phi}_i^4(K) - \frac{2^{-K}}{4} \sum_{n=0}^3 \sum_{k=0}^K (-1)^k \binom{K}{k} x_{i+k+n} \cos(2\phi_{i+n}) \\ &= \bar{\phi}_i^4(K) - 2^{-(K+2)} \sum_{n=0}^3 \Delta^{(K)} x_{i+n} \cos(2\phi_{i+n}) \\ &= \bar{\phi}_i^4(K) + \underbrace{2^{-(K+2)} (\Delta^{(K+1)} x_i + \Delta^{(K+1)} x_{i+2})}_{\epsilon_{P-BSC}} \cos(2\phi_i) \end{aligned} \quad (8)$$

where

$$\bar{\phi}_i^4(K) = 2^{-K} \sum_{k=0}^K \binom{K}{k} \left(\phi_{i+k} + \frac{1}{4} \sum_{n=0}^3 x_{i+k+n} \right). \quad (9)$$

Based on Eq. (8), it is clear that increasing K produces two main effects: first, the factor $2^{-(K+2)}$ exponentially decreases the harmonic amplitudes; second, higher-order difference terms (approach zero as K increases) occur in the harmonic amplitudes. Both effects significantly diminish the motion error.

Algorithm 1: P-BSC for motion error

Input:
 Binomial order: K .
 Phase-shifting step: $N = 3$ or 4 .
 Captured image sequence: $\{I_0, \dots, I_{N+K}\}$.
Output:
 Motion-error-free phase: $\tilde{\phi}_0(K)$.

```

1 for  $t \leftarrow 0$  to  $K$  do
2    $\tilde{\phi}_t(0) \leftarrow \begin{cases} \tan^{-1} \left( \frac{2I_{t+1} - I_t - I_{t+2}}{I_t - I_{t+2}} \right), N = 3 \\ \tan^{-1} \left( \frac{I_{t+1} - I_{t+3}}{I_t - I_{t+2}} \right), N = 4 \end{cases}$ 
3    $\tilde{\phi}_t(0) \leftarrow (\tilde{\phi}_t(0) + t \frac{\pi}{2}) \bmod (2\pi)$ 
4 end
5 for  $k \leftarrow 0$  to  $K - 1$  do
6   for  $i \leftarrow 0$  to  $K - k - 1$  do
7      $\tilde{\phi}_i(k+1) \leftarrow \tilde{\phi}_i(k) \oplus \tilde{\phi}_{i+1}(k)$ 
8   end
9 end
```

We noticed that the key reason for producing such a powerful error compensation effect is the use of $\pi/2$ phase shifting. Therefore, aside from the standard four-step phase shifting, three-step- $\pi/2$ phase shifting worths our consideration, the phase is computed as

$$\tilde{\phi}_i^3 = \tan^{-1} \left(\frac{2I_{i+1} - I_i - I_{i+2}}{I_i - I_{i+2}} \right), \quad (10)$$

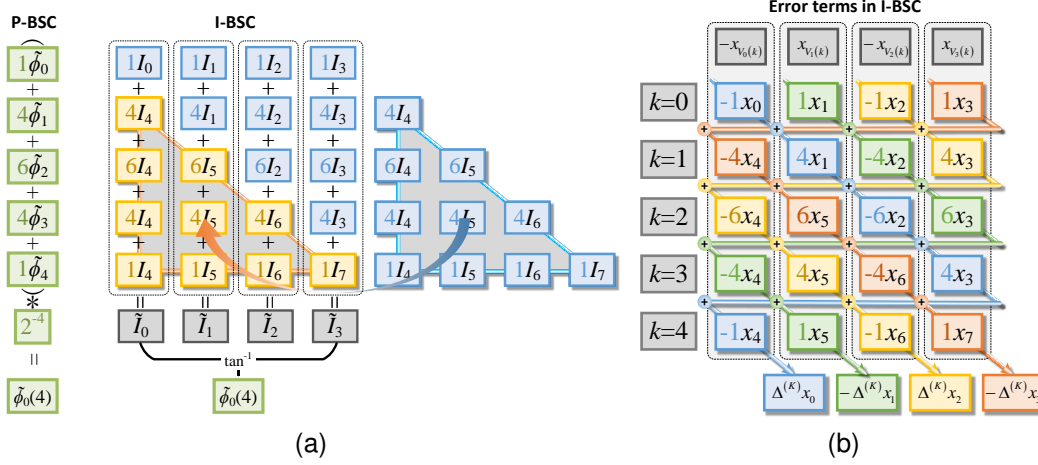


Fig. 5. Diagram of I-BSC. (a) our I-BSC sums the homogeneous fringe images, weighted by binomial coefficients, to generate four compensated fringe images, and then compute the motion-error-free phase. The arctangent function is computed only once. (b) The sum of the error terms along the diagonal direction precisely yields the high-order difference (Eq. (20) to Eq. (21)).

please note that the “three-step phase-shifting” discussed in this paper differs slightly from the standard three-step phase-shifting, as the phase shifting is $\pi/2$ instead of the traditional $2\pi/3$. Then we can derive the error compensation result as

$$\begin{aligned} \tilde{\phi}_i^3(K) &= \bar{\phi}_i^3(K) - 2^{-(K+2)} \Delta^{(K+2)} x_{i+2} \cos(2\phi_i) \\ &\quad + 2^{-(K+2)} \left(\Delta^{(K+1)} x_{i+2} + \Delta^{(K+1)} x_{i+1} \right) \sin(2\phi_i), \end{aligned} \quad (11)$$

where

$$\bar{\phi}_i^3(K) = 2^{-K} \sum_{k=0}^K \left[\binom{K}{k} (\phi_{i+K-k} + \delta_{i+K-k}^3) \right]. \quad (12)$$

Therefore, similar error compensation performance as four-step case is achieved. In practice, the weighted summation in Eq. (5) is difficult to implement in the algorithm aspect due to the ambiguity of the wrapped phase. To address this issue, instead of directly assigning weights, we decompose Eq. (5) into a pyramid-like procedure of adding up the successive two frames layer by layer, as shown in Fig. 4. In order to rectify the phase order error that occurs around the phase jumping area, we define the \oplus operator as

$$\phi_a \oplus \phi_b := \begin{cases} 0.5(\phi_a + \phi_b), & |\phi_a - \phi_b| > \pi \\ 0.5(\phi_a + \phi_b) + \pi, & |\phi_a - \phi_b| < \pi \end{cases} \quad (13)$$

This operation automatically compensates for the phase order error as long as the phase difference is greater than π . It is clear that our BSC strategy in this section works on the successive phase frames and is thus called phase-sequential BSC (P-BSC). The motion-error-free phase $\tilde{\phi}_i(K)$ can be obtained by performing our P-BSC, which is summarized as Algorithm 1, where “mod” represents modular operation. Note that we have corrected the constant phase shifting before adding up two phase frames $\tilde{\phi}_i(0)$ and $\tilde{\phi}_{i+1}(0)$. The MATLAB code for implementing P-BSC is open sourced at <https://github.com/GeyouZhang/BSC2.0>.

C. Image-sequential Binomial Self-Compensation

Although P-BSC effectively suppresses motion errors, it faces two challenges: high computational overhead and error accumulation, arising from the need to calculate multi-frame phases and perform weighted summation. In this paper, inspired by P-BSC, we propose a novel image-sequential BSC (I-BSC) that computes the arctangent function only once, addressing both challenges.

Our I-BSC is inspired by the idea of weighted sum using binomial coefficients in the P-BSC. Instead of summing up the **phase frames**, our I-BSC adds up the homogeneous **fringe images** weighted by the binomial coefficients, from which four compensated fringe images $\tilde{I}_0, \tilde{I}_1, \tilde{I}_2, \tilde{I}_3$ are obtained as shown in Fig. 5(a). Note that homogeneous fringe images mean the encoded frames with the same trigonometric function name and polarity. For example, $I_{4n}, I_{4n+1}, I_{4n+2}, I_{4n+3}$ are four groups of homogeneous fringe images, where $n \in \mathbb{N}$. The four compensated fringe images are computed as

$$\tilde{I}_m = \sum_{k=0}^K \binom{K}{k} I_{V_m(k)}, \quad (14)$$

where the index vector is

$$V_m(k) = (k+3) - [(k+3-m) \bmod 4], \quad (15)$$

where $m \in 0, 1, 2, 3$ represents the group number of homogeneous fringe images. Finally, only one arctangent function is employed to compute the motion-error-free phase as

$$\tilde{\phi}_0(K) = \tan^{-1} \left(\frac{\tilde{I}_1 - \tilde{I}_3}{\tilde{I}_0 - \tilde{I}_2} \right). \quad (16)$$

An additional advantage of using I-BSC is that the ripple-error-free modulation image B can be facily computed as

$$B = 2^{-(K+1)} \sqrt{(\tilde{I}_1 - \tilde{I}_3)^2 + (\tilde{I}_0 - \tilde{I}_2)^2}, \quad (17)$$

while P-BSC does not provide a method for calculating B .

The I-BSC framework is so simple that it can be described using just two equations (i.e., Eq. (14) and (16)). In fact, the I-BSC algorithm is not derived from mathematical formulas but is entirely inspired by the intuitive idea of using binomial coefficients to weight and sum in P-BSC. We generalize the BSC concept from phase sequences to image sequences.

Surprisingly, as shown in our following analysis, we find that the theoretical error of I-BSC is identical to that of 4-step P-BSC. Meanwhile, the required number of arctangent function calculations is reduced from K to 1, significantly improving the computation speed.

To model the error of I-BSC, considering a small phase-shift error $x_{V_m(k)}$, we have $\sin(x_{V_m(k)}) \approx x_{V_m(k)}$ and $\cos(x_{V_m(k)}) \approx 1$. Subsequently, we rewrite Eq. (1) as

$$I_{V_m(k)} = A + B \cos(\phi_{V_m(k)}) - Bx_{V_m(k)} \sin(\phi_{V_m(k)}). \quad (18)$$

Since there are numerous index variables involved in this section, we will focus on the computation of the phase for frame 0. The calculation and analysis for frame i follow a similar approach. Then we substitute Eq. (18) into Eq. (16) to have

$$\begin{aligned} \tilde{\phi}_0(K) &= \tan^{-1} \left(\frac{\sum_{k=0}^K \binom{K}{k} (I_{V_3(k)} - I_{V_1(k)})}{\sum_{k=0}^K \binom{K}{k} (I_{V_2(k)} - I_{V_0(k)})} \right) \\ &= \tan^{-1} \left(\frac{\sin(\phi_0) + 2^{-(K+1)} \sum_{k=0}^K \binom{K}{k} (x_{V_3(k)} + x_{V_1(k)}) \cos(\phi_0)}{\cos(\phi_0) - 2^{-(K+1)} \sum_{k=0}^K \binom{K}{k} (x_{V_2(k)} + x_{V_0(k)}) \sin(\phi_0)} \right). \end{aligned} \quad (19)$$

Thus, the motion error of I-BSC is expressed as

$$\begin{aligned} \epsilon_{\text{I-BSC}} &= \tilde{\phi}_0(K) - \phi_0 \\ &= \tan^{-1} \left(\frac{\sum_{k=0}^K \binom{K}{k} (x_{V_3(k)} + x_{V_1(k)}) \cos^2(\phi_0) + \sum_{k=0}^K \binom{K}{k} (x_{V_2(k)} + x_{V_0(k)}) \sin^2(\phi_0)}{2^{K+1} + \sum_{k=0}^K \binom{K}{k} [(x_{V_3(k)} + x_{V_1(k)}) - (x_{V_2(k)} + x_{V_0(k)})] \sin(\phi_0) \cos(\phi_0)} \right), \\ &\approx 2^{-(K+2)} \sum_{k=0}^K \binom{K}{k} \left[\sum_{m=0}^3 x_{V_m(k)} + (-x_{V_0(k)} + x_{V_1(k)} - x_{V_2(k)} + x_{V_3(k)}) \cos(2\phi_0) \right] \\ &:= 2^{-(K+2)} \sum_{k=0}^K \binom{K}{k} (-x_{V_0(k)} + x_{V_1(k)} - x_{V_2(k)} + x_{V_3(k)}) \cos(2\phi_0) \end{aligned} \quad (20)$$

note that we overlook the DC component of the error because it does not significantly affect the reconstruction results. It is difficult to straightforwardly derive a concise error expression from Eq. (20). Let's list the cases for $k = 0 \sim 4$ in Fig. 5(b) to more intuitively display the error terms in I-BSC. When the error terms are summed along the diagonal direction, rather than row-by-row or column-by-column, as illustrated in Fig. 5(b), the high-order-form error terms are immediately obtained. This idea is inspired by the observation that $V_{m+1}(k+1) \equiv V_m(k) + 1$. Ultimately, Eq. (20) is simplified into

$$\begin{aligned} \epsilon_{\text{I-BSC}} &= 2^{-(K+2)} \sum_{k=0}^K (-1)^k \binom{K}{k} (-x_k + x_{k+1} - x_{k+2} + x_{k+3}) \cos(2\phi_0) \\ &= 2^{-(K+2)} (-1)^K \sum_{k=0}^K (-1)^{K-k} \binom{K}{k} (-x_k + x_{k+1} - x_{k+2} + x_{k+3}) \cos(2\phi_0) \\ &= 2^{-(K+2)} (-1)^K \left(\Delta^{(K+1)} x_0 + \Delta^{(K+1)} x_2 \right) \cos(2\phi_0) \end{aligned} \quad (21)$$

At first glance, a comparison of the theoretical expressions in Eq. (8) and Eq. (21) indicates that I-BSC and P-BSC exhibit the same performance in motion error suppression. However, in reality, I-BSC does not sum phase frames up, thereby avoiding error accumulation induced by approximation of $\tan(\cdot) \approx \cdot$ in Eq. (4), whereas P-BSC retains the residual

errors. As a result, I-BSC is of faster error convergence than P-BSC as K increases, which will be verified and elaborated on in simulations and real-world experiments in Section VI. The I-BSC procedure is summarized as Algorithm 2. The MATLAB code for implementing I-BSC is open sourced at <https://github.com/GeyouZhang/BSC2.0>.

Algorithm 2: I-BSC for motion error**Input:**Binomial order: K .Captured image sequence: $\{I_0, \dots, I_{K+4}\}$.**Output:**Motion-error-free phase: $\tilde{\phi}_0(K)$.

```

1 for  $m \leftarrow 0$  to 3 do
2    $\tilde{I}_m \leftarrow 0$ 
3   for  $k \leftarrow 0$  to  $K$  do
4      $V_m(k) \leftarrow (k+3) - [(k+3-m) \bmod (4)]$ 
5      $\tilde{I}_m \leftarrow \tilde{I}_m + \binom{K}{k} I_{V_m(k)}$ 
6   end
7 end
8  $\tilde{\phi}_0(K) \leftarrow \tan^{-1} \left( \frac{\tilde{I}_1 - \tilde{I}_3}{\tilde{I}_0 - \tilde{I}_2} \right)$ 

```

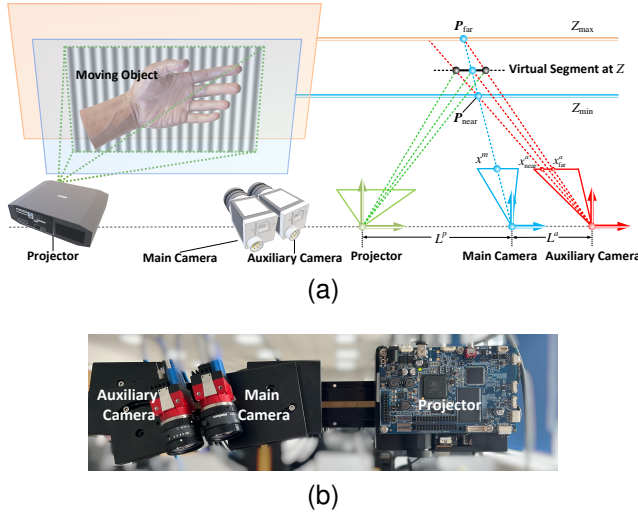


Fig. 6. (a) Diagram of our paraxial binocular structured light system, and (b) experimental setup..

V. PARAXIAL STEREO PHASE UNWRAPPING

Stereo phase unwrapping (SPU) can recover the unambiguous absolute phase based on multi-view geometry cues, thereby achieving 3D reconstruction with single-frequency fringe patterns. Consequently, SPU is widely employed in dynamic PSP [27], [33], [50]–[52]. However, to ensure robust phase unwrapping, the common methods adopted are to either increase the number of views [51] or set a quite limited baseline between camera and projector [27], [51]. The former causes increased hardware costs and the latter reduces the accuracy of 3D imaging.

Firstly, as depicted in Fig. 6(a), we tailor a paraxial binocular structured light system that intentionally sets a very short baseline between two cameras to achieve a narrow disparity range, ensuring the use of high-frequency fringes, while maintaining the baseline between the main camera and projector is long enough for adequate accuracy.

Secondly, by introducing uniqueness and correctness constraints that jointly determine the feasible region of fringe frequency f , camera-camera baseline L^a , and camera-projector baseline L^p , we provide clear guidance for system setup and fringe frequency selection as shown in Fig. 7.

Finally, we propose paraxial stereo phase unwrapping with

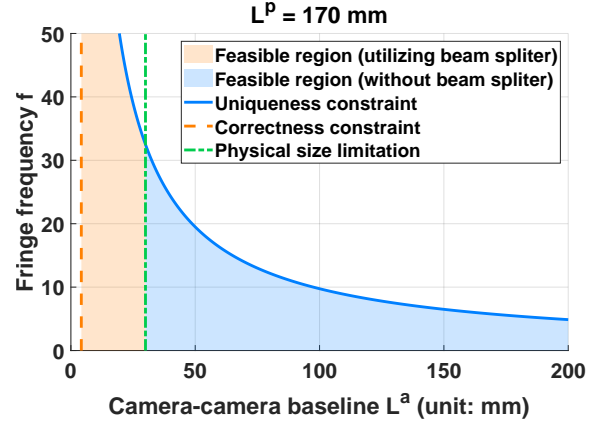


Fig. 7. The uniqueness constraint, correctness constraint, and physical size limitations of cameras are considered when selecting the fringe frequency. We assign the physical size limitation as 30 mm, $L^p = 170$ mm and $G = 0.02 \text{ DN/e}^-$ for demonstration.

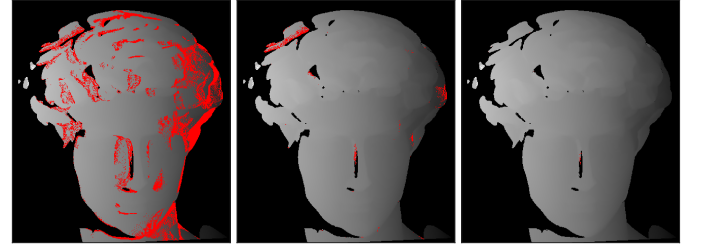


Fig. 8. The phase outliers (marked in red) are corrected as the iteration steps r of HA increase. Left: $r = 0$ (raw noisy phase), middle: $r = 1$, right: $r = 2$.

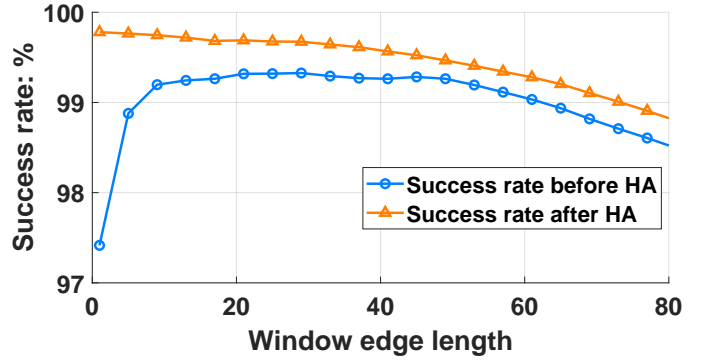


Fig. 9. Window size of stereo matching verses success rate of phase unwrapping

hierarchical adjustment to remove the phase outliers induced by wrong stereo matching results, obtaining robust 3D reconstruction for complex surfaces. We adopt sum of absolute difference algorithm to conduct stereo matching on the wrapped phase map of the main and auxiliary camera, which is computationally efficient but noisy. To correct the phase outliers, motivated by [53] and [54], we propose a hierarchical adjustment (HA) method for phase outlier to eliminate the phase unwrapping errors. HA repeats the rectification [53] of unwrapping errors for r times to comprehensively correct the outliers. Figure 8 shows the phase outliers are corrected as the iteration steps r of HA increase, and thus we empirically propose to set $r = 2$ to achieve a trade-off between effectiveness

and efficiency. We recommend using a single pixel window (1×1) for stereo matching on the wrapped phase map, as this results in a higher success rate (SR) for the final absolute phase obtained by HA as shown in Fig. 9.

In summary, utilizing the PSPU enable the achievement of unambiguous 3D reconstruction within the specified depth range, using only a single set of high-frequency fringe patterns. As a result, we can employ the cyclic projection strategy [27] to facilitate the implement of our BSC for dynamic 3D scanning. The implementation details can be found in the supplementary materials and the MATLAB code is open sourced at <https://github.com/GeyouZhang/BSC2.0>.

VI. EXPERIMENTAL EVALUATIONS

The proposed algorithm is implemented on an Intel(R) Core(TM) i7-13790F @ 2.10 GHz with 32 GB RAM. Our experimental system (Fig. 6(b)) consists of two AVT 1800U-120c cameras that have 1280×960 resolution, equipped with 8 mm Computar lenses, and a TI DLP4500 projector with a resolution of 912×1140 . We cropped the cameras' field of view to 640×480 to have a 90 fps image acquisition speed. The two cameras are synchronized by the trigger signal from the projector.

A. Frame Rate of BSC

TABLE I
COMPARING THE COMPUTATION COMPLEXITY.

Operation	P-BSC	I-BSC
\tan^{-1}	$K + 1$	1
mod	$(0.5K + 1)(K + 1)$	0
$+/-$	$(0.5K + 4)(K + 1)$	$4K + 2$
\times/\div	$K(K + 1)$	$4K$
cmp*	$0.5K(K + 1)$	0

All operations are pixel-wise, which means the total number of computation needs to be multiplied by the number of pixels in the image.

*: Comparison operation.

Due to avoiding multi-frame phase calculations and layer by layer accumulation in P-BSC, our I-BSC exhibit significant advantage in computation complexity as summarized in Table. I. Our I-BSC remarkably diminishes all kinds of operations including \tan^{-1} , mod, $+/-$, \times/\div , and cmp, reducing the time complexity by at least one polynomial order.

To demonstrate the speed advantage of I-BSC, we implemented both P-BSC and I-BSC using single-threaded C++ code and ran the programs on an Intel i7-13790F CPU at 2.10 GHz. We conducted experiments for both I-BSC and P-BSC with binomial orders ranging from 0 to 15, performing each operation 100 times. The average computation frame rates are presented in Fig. 10. It is evident that I-BSC accelerates P-BSC by several to tens of times, achieving frame rates exceeding 50 fps when $K < 5$ even with CPU single-threaded programming. The frame rate improvement increases linearly with the binomial order, indicating that I-BSC reduces the time complexity of P-BSC by one polynomial order.

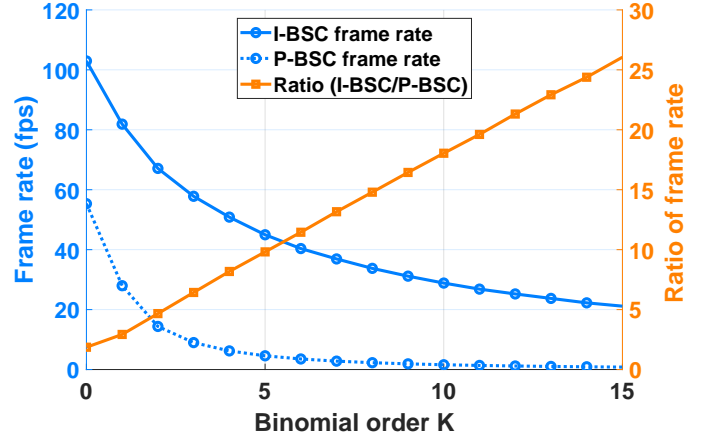


Fig. 10. Comparison of I-BSC and P-BSC in computation frame rate. As the binomial order (number of input images) increases, the speed advantage of I-BSC over P-BSC becomes increasingly significant.

B. Convergence Speed of Motion Error in P-BSC and I-BSC

1) *Simulations*: We conducted simulations to compare the performance of P-BSC and I-BSC. In our simulation, we assume the dynamic phase shifting error x_i presents a uniform acceleration motion with $v_0 = 0.25$ rad/s and $a = 0.01$ rad/s². As shown in row 1 of Fig. 11, the motion error of I-BSC rapidly converges at a faster rate than exponential decay with base 2. This observation is consistent with the prediction in Eq. (21), which states that due to the combined effects of exponential decay coefficients and higher-order differences, motion errors exhibit a faster convergence rate than exponential decay with base 2. Meanwhile, the motion errors in both the 3-step and 4-step P-BSC also decay quickly but exhibit noticeable residual harmonic errors. This is because the approximation $\tan(\cdot) \approx \cdot$ in Eq. (3) is applied K times in the error analysis of P-BSC (Eq. (6)), resulting in higher-order residual errors when summing. As a result, P-BSC suffers from error accumulation, preventing it from achieving its theoretical accuracy. However, the error accumulation issue does not exist in I-BSC as the approximation is applied only once during the error analysis, and thus Eq. (21) accurately describes the error convergence.

Moreover, we evaluated the impact of slight nonlinearity on BSC performance by setting $\gamma = 1.15$, with the results shown in row 2 of Fig. 11. The error suppression capabilities of both P-BSC and I-BSC are impaired in the presence of nonlinearity. Specifically, 3-step P-BSC is significantly affected and is not recommended for this scenario. However, the motion errors in I-BSC and 4-step P-BSC maintain exponential decay when the number of patterns is less than 8, indicating that they retain effective performance in high-speed scenarios.

In conclusion, our simulation results indicate that: 1) in the absence of nonlinearity, I-BSC outperforms P-BSC and reduces motion error at a rate faster than exponential decay with base 2; 2) I-BSC and 4-step P-BSC exponentially reduce motion error, even in the presence of slight nonlinearity; and 3) the use of non-linear correction algorithms is recommended to further enhance the performance of both P-BSC and I-BSC.

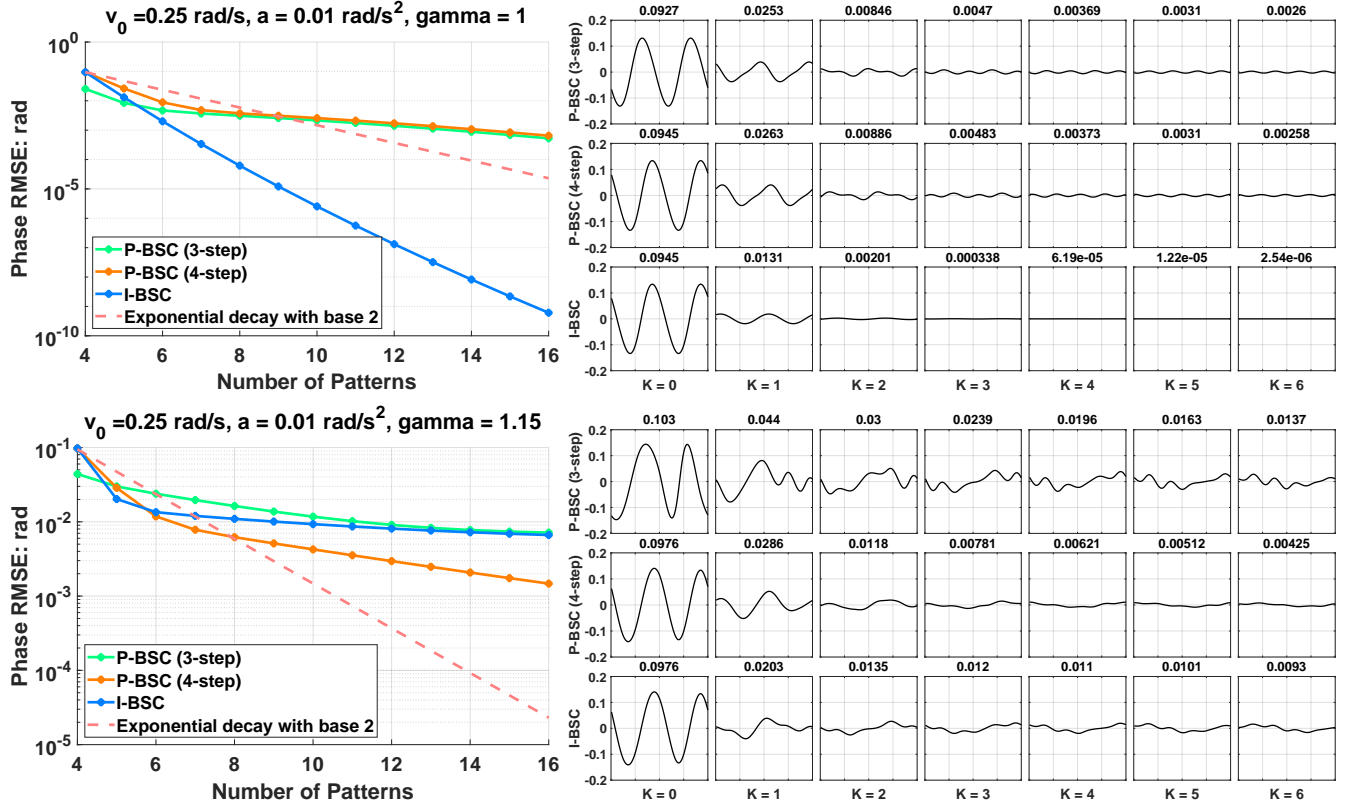


Fig. 11. Simulation of motion-induced phase errors in P-BSC and I-BSC: Row 1: linear case; Row 2: nonlinear case with $\gamma = 1.15$. The RMSE is labeled above each subfigure.

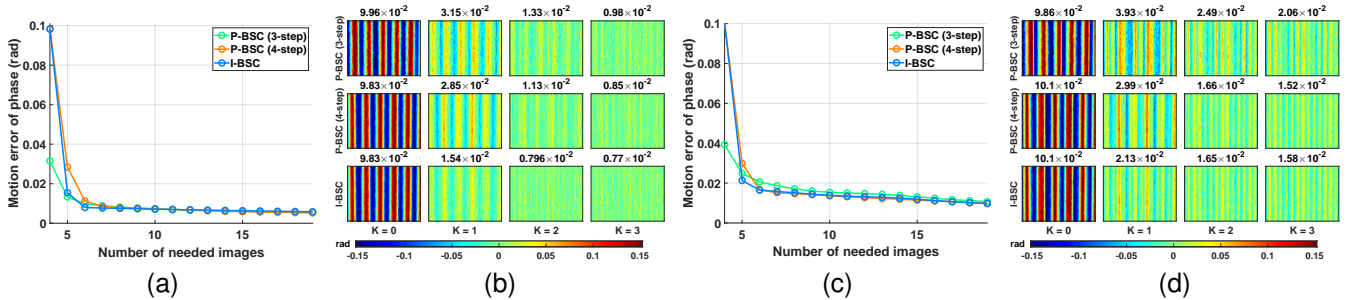


Fig. 12. Real-world experiment on motion-induced phase error of P-BSC and I-BSC. The mean absolute error (MAE) of phase labeled above each sub-figure exponentially diminishes as K increases. (a) and (b) the results with FNR to rectify nonlinearity; (c) and (d) the results without FNR to rectify nonlinearity.

2) *Real-world Experiments*: We measured a flat plate moving towards the camera using our 3-step P-BSC, 4-step PBSC, and I-BSC. We conducted experiments separately with and without our FNR to rectify nonlinearity. The results visualized in Fig. 12 are consistent with our error analysis and simulations. It can be seen that P-BSC and I-BSC significantly reduce the ripples induced by motion with the increment of K . $K = 0$ represents the raw phase without any error compensation. Moreover, I-BSC can better suppress motion error than 3-step and 4-step P-BSC when adopting the same binomial order K , indicating its fast convergence speed. The nonlinear error compromises the performance of both P-BSC and I-BSC, in which the 3-step P-BSC is the most susceptible one. Therefore, in the presence of nonlinearity, we recommend performing nonlinearity correction before using

BSC, otherwise, choose I-BSC or 4-step P-BSC rather than 3-step P-BSC to have a robust performance. Note that the binomial order K can be flexibly chosen according to the accuracy and time efficiency requirements. In the following real-world experiments in Section. VI-C, VI-D, VI-E, VI-F, we adopted eight images ($K = 4$) to sufficiently suppress both motion error and intensity noise. In this case, P-BSC and I-BSC exhibit nearly identical performance, as shown in Fig. 12. Therefore, unless otherwise specified, BSC refers to the results of P-BSC in Section. VI-C, VI-D, VI-E, VI-F. We omit showing the results of I-BSC in the graphics, as the point clouds of P-BSC and I-BSC are visually indistinguishable.

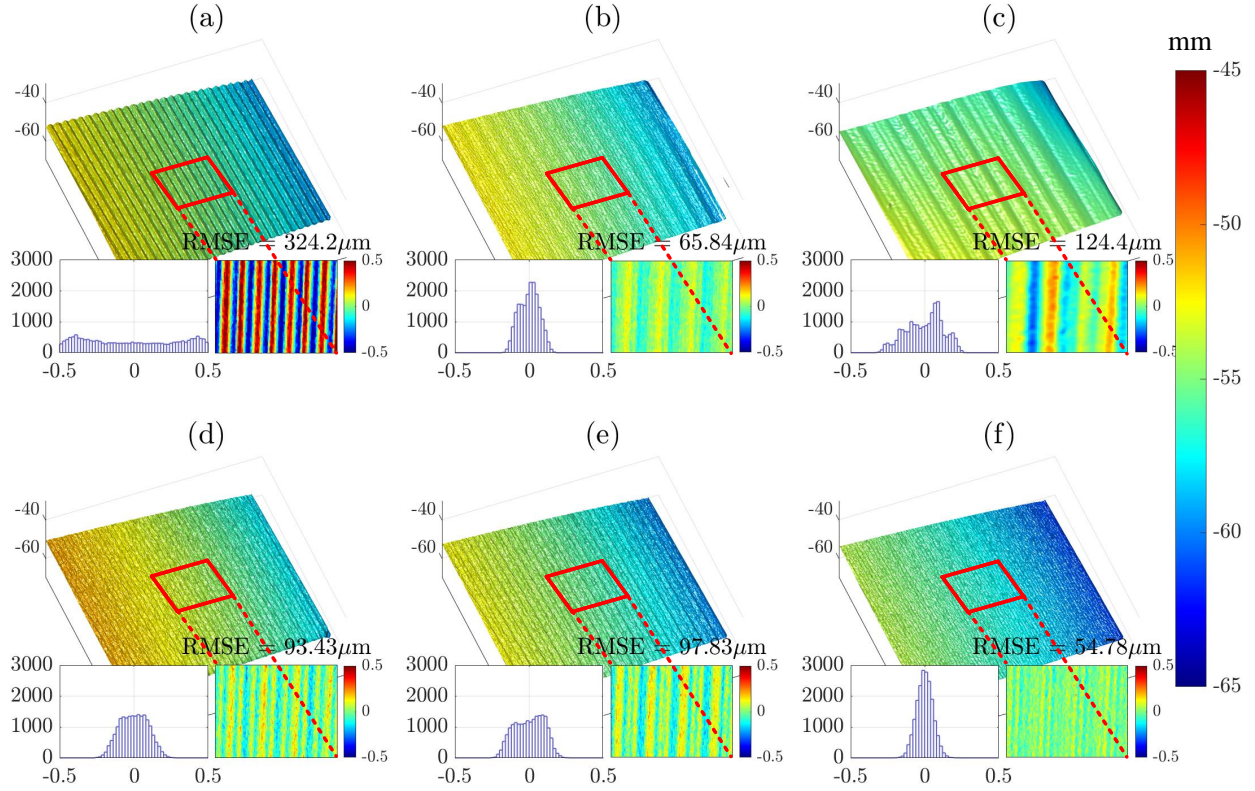


Fig. 13. Measurement results of a moving flat plane by (a) traditional four-step phase shifting, (b) HTC [41], (c) μ -FTP [48], (d) PFD [36], (e) PFS [43], and (f) our BSC.

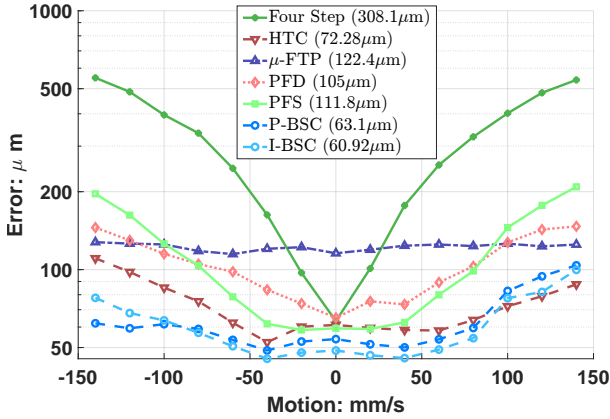


Fig. 14. Measurement error VS motion speed of a periodically waving plate by traditional four-step phase shifting, HTC [41], μ -FTP [48], PFD [36], PFS [43], and our P-BSC/I-BSC, the value in parentheses represents the mean error. Note the y-axis is in logarithmic scale.

C. High Depth Resolution

We measured a periodically waving plate at a distance of 500 mm by using our BSC (8 frames) and five representative methods for comparison: 1) traditional four-step PSP (4 frames), 2) Hilbert transform compensation (HTC, 4 frames) [41], 3) micro Fourier transform profilometry (μ -FTP, 4 frames) [48], 4) phase frame difference method (PFD, 8 frames) [36], 5) phase frame sum method (PFS, 5 frames) [43]. The fringe wavelength was set to 24 pixels for the cyclic $\pi/2$ phase shifting patterns and was set to [22, 24, 26] for μ -FTP.

The plate moves within a distance range of [400, 500] mm and a speed range of [-150, 150] mm/s, and our measurement lasted for 800 frames (about 8.9 seconds). We select three 160×120 rectangular windows in each depth map and fit the quadric surface as the ground truth, then we compute the root mean squared error (RMSE) within the selected regions. The trend of RMSE changing with motion speed is depicted in Fig. 14. The results show that both P-BSC and I-BSC exhibit nearly identical performance in mitigating motion error, surpassing existing methods.

Then we selected a moment when the speed of the plate was -88 mm/s, and depict the reconstructed point clouds in Fig. 13, our BSC effectively reduces the motion error from $324.2 \mu\text{m}$ to $54.78 \mu\text{m}$ compared with traditional four-step phase shifting. By counting the histogram of errors, it can be observed that the error distribution of our BSC visually presents a normal distribution, which means Gaussian noise (induced by unstable ambient light, camera/projector flicker, quantization error, and sensor noise of the camera and projector) is the main component of error. In other words, the motion error is effectively suppressed by BSC. Meanwhile, the error distribution of other methods deviates from the normal distribution, indicating the existence of residual errors.

D. High Pixel Resolution

PSP's pixel-wise characteristic is one of its most crucial merits. Our BSC maintains this property, thereby exhibiting robustness to complex surface or depth discontinuous scenes.

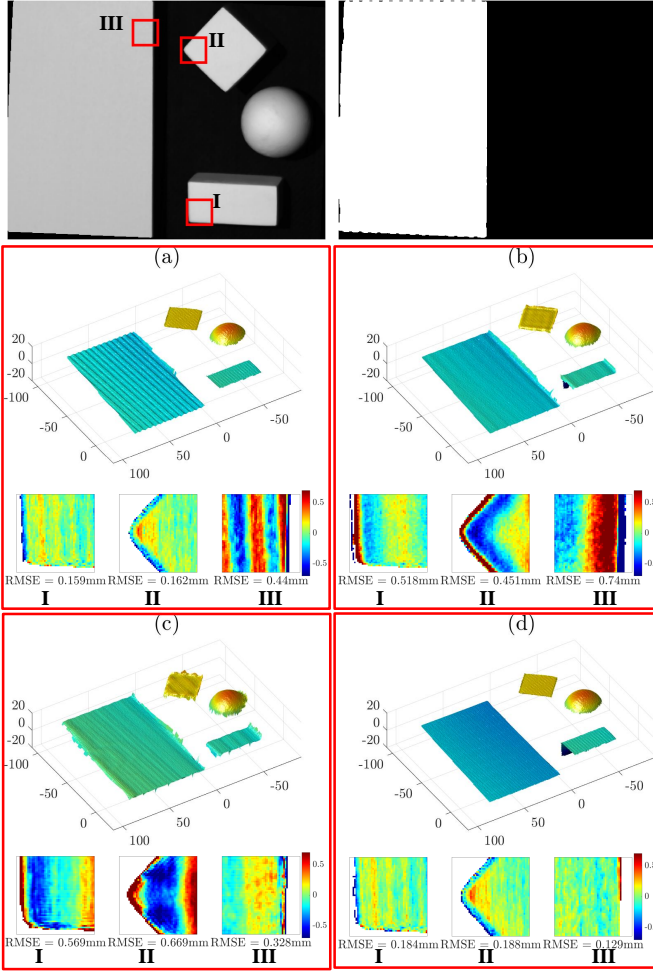


Fig. 15. Depth discontinuous scene (top left) and motion area labeled in white (top right). Reconstruction results and error at edges: (a) traditional four-step phase shifting, (b) HTC [41], (c) μ -FTP [48], and (d) our BSC.

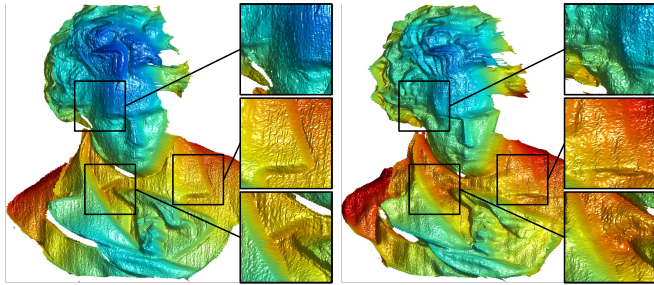


Fig. 16. Scanning a moving statue. Left: BSC and right: HTC.

We set up a scene with three static gypsum geometries and one moving plate. Then we employed our BSC, μ -FTP, and HTC. The results are shown in Fig. 15. It can be seen that the two non-pixel-wise methods, i.e., μ -FTP and HTC, exhibit visible deformation to the naked eye in the point cloud around the depth jumping areas. We selected three rectangular windows and quantitatively evaluate the RMSE, the results show that the RMSE of non-pixel-wise methods is significantly greater than our BSC. Moreover, we scanned a moving statue using BSC and HTC to compare the performance on complex surfaces.

The results are shown in Fig. 16. The result of HTC shows the details at the collar of the coat and shirt are smoothed and the profile near the temple is unnaturally deformed, whereas our BSC correctly reconstructs the statue.

It can be seen that, by conducting global operators on the captured images, i.e., Fourier transform or Hilbert transform, μ -FTP and HTC are effective in mitigating motion error, yet inevitably causing spectrum truncation, thereby inducing Gibbs phenomenon at edges. Therefore, we can conclude that our BSC with pixel-wise property is more robust compared with non-pixel-wise methods when dealing with complex surface or depth discontinuous scenes, showcasing strong resolving ability in detail.

E. High Temporal Resolution

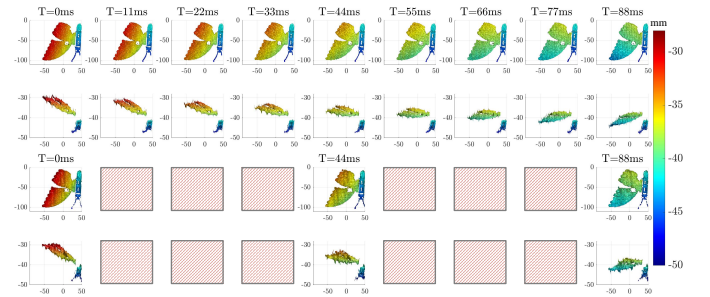


Fig. 17. The measurement result of a wooden butterfly with wings flapping, during $T=0\text{ ms} \sim 88\text{ ms}$, Row 1 and 2: our BSC; Row 3 and 4: μ -FTP [48].

Our BSC employs cyclic $\pi/2$ phase-shifting fringe patterns, any $K + N$ successive captured images can be used for reconstructing one frame of 3D point clouds. Therefore, our resulting frame rate of 3D point clouds is the same as the camera frame rate, thereby achieving a high temporal resolution of the measurement. That is the frame-wise loopable property we mentioned in the introduction. We successively conducted BSC and μ -FTP to measure a wooden butterfly with wings flapping cyclically, and then manually aligned the timeline, the results are shown in Fig. 17. We noticed that our method can achieve 3D reconstruction with a frame rate of 90 fps (the same as the camera acquisition speed), while μ -FTP reconstructing at 30 fps. Thus, our method is capable of distinguishing tinier motions.

F. Performance on Non-rigid or Multiple Objects

To demonstrate the generality of BSC, we employ traditional four-step PSP and BSC (8 images) with fringe wavelength of 36 pixels to scan various dynamic scenes, including 1) rigid object: moving gypsum statues of David and Mozart; 2) non-rigid object: fluttering tissue and waving human hand; 3) multiple object: combination 1 (flapping wooden butterfly and moving statue) and combination 2 (flapping paper wing and moving plate), and the results are shown in Fig. 18. We captured 400 image frames (about 4 seconds) employing our pipeline. The complete motion process video can be found in the supplementary materials. We observed that BSC can effectively eliminate the severe ripple errors caused by object

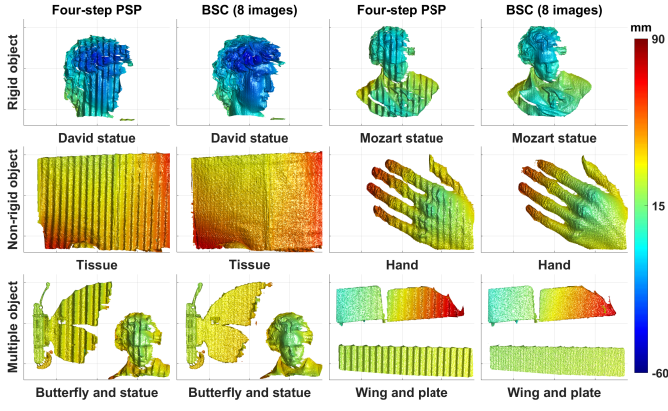


Fig. 18. The measurement results of three types of dynamic objects. **Row 1:** rigid objects, **Row 2:** non-rigid objects, **Row 3:** multiple objects.

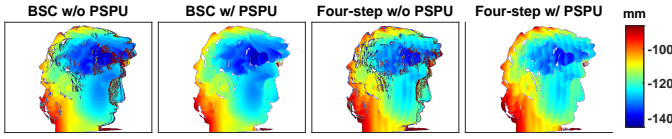


Fig. 19. Depth map with/without PSPU. When the depth range is too wide, PSPU can effectively rectify the outliers in phase unwrapping.

motion, even in non-rigid and multiple-object scenes, because our BSC processes each pixel individually rather than relying on a local or global consistent parameter to compensate for motion errors. Furthermore, when the depth range is too wide, a large number of outliers occurred in our previous work due to incorrect stereo matching. In this paper, this issue has been addressed by utilizing our PSPU as shown in Fig. 19.

G. Intensity Noise Suppression Ability

In a practical FPP system, the intensity of the fringe pattern at each point of the object is acquired by a digital camera and inevitably contaminated by intensity noise [9]. The intensity noise ω_n in each captured image originates from various error sources, such as unstable ambient light, projector illumination noise, camera noise, mechanical vibration, etc. According to the central limit theorem, the intensity noise of the captured image can be modeled as an additive Gaussian white noise with zero mean and a variance of σ^2 [55], [56]

$$\sigma^2 = \sigma_{dark}^2 + G(I - I_{dark}), \quad (22)$$

where I_{dark} and σ_{dark} represents the dark signal and its variance, G is the camera system gain. Then we can have the variance of Gaussian noise in N -step PSP is [56]

$$\sigma_{\phi}^2(N) = \frac{2}{NB^2} [\sigma_{dark}^2 + G(A - I_{dark})] \approx \frac{2G}{NB}. \quad (23)$$

We find that it's difficult to derive a simple form noise model for our P-BSC and I-BSC, thus we conduct a simulation to compare K -order P-BSC and I-BSC with N -step PSP in terms of intensity noise suppression ability, as shown in Fig. 20 (we maintain that $K = N - 4$ holds true). Consequently,

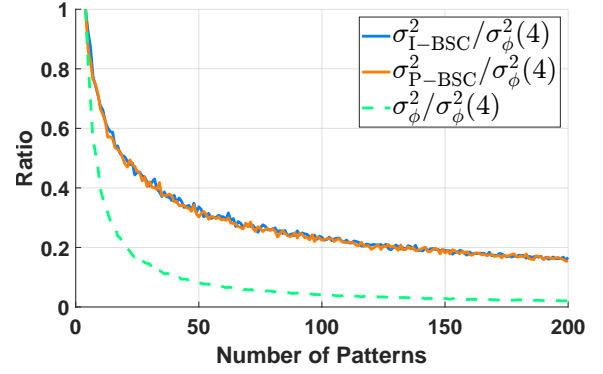


Fig. 20. The comparison of intensity noises among P-BSC, I-BSC, and traditional N -step PSP.

we conduct curve fitting to approximately have a empirical formula as

$$\sigma_{I-BSC}^2(N) = \sigma_{P-BSC}^2(N) \approx \frac{G}{\sqrt{NB}}, \quad (24)$$

note that N represents the number of patterns used by P-BSC and I-BSC.

The results show that, P-BSC and I-BSC equivalently mitigate the intensity noise as binomial order K increases, but the noise suppression effects are weaker than traditional N -step PSP. Blindly increasing K is uneconomical in reducing intensity noise. Therefore we empirically propose to adopt $K = 4$ (8 patterns) for dynamic 3D scanning, which can significantly suppress motion error while also reducing intensity noise.

H. Ease of Deployment

In this paper, we tailor a paraxial binocular structured light system that projects single-frequency fringe patterns, achieving unambiguous phase unwrapping. In addition to the single-frequency scheme, our I-BSC and P-BSC are easy to deploy with popular temporal phase unwrapping techniques, as they do not require any novel or customized patterns. We performed simulations to demonstrate that the I-BSC and P-BSC can be easily applied to hierarchical phase unwrapping [57], three-frequency heterodyne phase unwrapping [25], and number-theory-based phase unwrapping [58], resulting in reduced motion errors and unwrapping failures. To implement our BSC method, the pattern projection order is slightly adjusted, as shown in Fig. 21. The fringe patterns for each frequency are uniformly distributed throughout the time series.

We assume the dynamic phase shifting error x_i presents a uniform acceleration motion with $v_0 = 0.15$ rad/s and $a = 0.005$ rad/s². In dynamic scenes, the ripple-like motion error reduces the success rate (SR) of temporal phase unwrapping methods, leading to numerous outliers, as illustrated in Fig. 22. After applying our P-BSC or I-BSC methods, the motion error is significantly reduced, ensuring correct unwrapping results. Table II lists the SR of three temporal phase unwrapping methods after implementing K -order BSC. It is evident that the SR improves significantly as K increases. When $K \geq 3$ is adopted, most phase unwrapping failures are eliminated. Thus, considering the ease of deployment, BSC

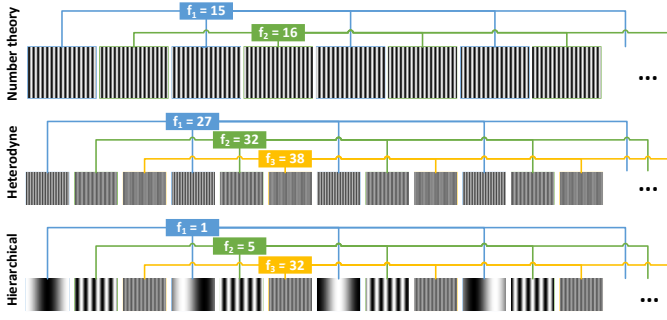


Fig. 21. The illustration of pattern projection strategy when applying BSC to hierarchical, three-frequency heterodyne, and number-theory-based phase unwrapping.

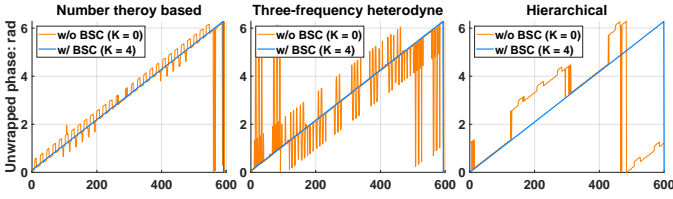


Fig. 22. In our simulation of dynamic scenes, number-theory-based, three-frequency heterodyne, and hierarchical unwrapping yield numerous outliers due to the motion error. By applying BSC to the temporal phase unwrapping methods, the outliers are substantially eliminated.

TABLE II

SUCCESS RATE OF NUMBER-THEORY-BASED, THREE-FREQUENCY HETERODYNE, AND HIERARCHICAL PHASE UNWRAPPING METHODS AFTER APPLYING P-BSC AND I-BSC. BINOMIAL ORDER EQUAL TO ZERO REPRESENTS THE RAW METHODS. (UNIT: %)

Binomial order	Number theory		Heterodyne		Hierarchical	
	P-BSC	I-BSC	P-BSC	I-BSC	P-BSC	I-BSC
0	53.91		67.89		39.10	
1	79.37	88.19	94.34	100.00	35.94	33.44
2	99.00	100.00	100.00	100.00	63.56	99.67
3	100.00	100.00	100.00	100.00	100.00	100.00
4	100.00	100.00	100.00	100.00	100.00	100.00

is not only applicable to our system, but can also be used in more universal structured light systems. We believe that various temporal and spatial phase unwrapping methods could benefit from our BSC strategy, resulting in fewer outliers and higher accuracy when applied to dynamic scenes.

VII. CONCLUSIONS AND FUTURE OUTLOOK

This paper investigates the mechanism of motion error in PSP. Upon that, we propose a phase-sequential binomial self-compensation (P-BSC) to exponentially reduce the motion error in a pixel-wise and frame-wise loopable manner. Further, we reveal two issues arising due to P-BSC's computation of multi-frame phases: high computational overhead and error accumulation. To address both issues, inspired by P-BSC, an image-sequential binomial self-compensation (I-BSC) is proposed, reducing the computational complexity of P-BSC by one polynomial order, while reaching faster motion error convergence. I-BSC generalizes the BSC concept from phase sequences to image sequences, fully inheriting the high depth-pixel-temporal resolution of P-BSC. Additionally, a paraxial

stereo phase unwrapping and full-chain rectification address the phase ambiguity and nonlinear issues that arise due to the limited number of patterns in dynamic scenes. Our P-BSC and I-BSC can be facily deployed with popular temporal and spatial phase unwrapping methods, resulting in fewer outliers and higher accuracy in dynamic scenes. Comprehensive analysis, simulations, and experiments not only provide detailed guidance for algorithm application but also show that the proposed P-BSC and I-BSC surpass existing methods in reducing motion error, enabling 3D reconstruction with high pixel-depth-temporal resolution.

We currently focus on reducing axial motion errors induced by motion along the camera's optical axis. In the future, we believe that by fine-tuning and integrating existing optical flow tracking algorithms, radial motion errors caused by movement orthogonal to the optical axis can also be effectively reduced. Moreover, we restrict the binocular baseline by positioning the cameras side by side, constrained by the physical dimensions of the industrial camera. In subsequent iterations, we plan to improve our prototype by integrating a beam splitter or using a customized binocular system to further reduce the binocular baseline. This adjustment will enable the utilization of fringe patterns with higher frequencies, thereby enhancing measurement accuracy.

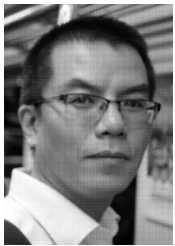
REFERENCES

- [1] J. Qian, S. Feng, M. Xu, T. Tao, Y. Shang, Q. Chen, and C. Zuo, "High-resolution real-time 360 degree 3d surface defect inspection with fringe projection profilometry," *Optics and Lasers in Engineering*, vol. 137, p. 106382, 2021.
- [2] J. Zhu, F. Yang, J. Hu, and P. Zhou, "High dynamic reflection surface 3d reconstruction with sharing phase demodulation mechanism and multi-indicators guided phase domain fusion," *Optics Express*, vol. 31, no. 15, pp. 25318–25338, 2023.
- [3] S. Logozzo, E. M. Zanetti, G. Franceschini, A. Kilpelä, and A. Mäkinen, "Recent advances in dental optics—part i: 3d intraoral scanners for restorative dentistry," *Optics and Lasers in Engineering*, vol. 54, pp. 203–221, 2014.
- [4] J. Geng, "Structured-light 3d surface imaging: a tutorial," *Advances in Optics and Photonics*, vol. 3, no. 2, pp. 128–160, 2011.
- [5] Y. Ye, H. Chang, Z. Song, and J. Zhao, "Accurate infrared structured light sensing system for dynamic 3d acquisition," *Applied Optics*, vol. 59, no. 17, pp. E80–E88, 2020.
- [6] Z. Wu and Q. Zhang, "High-speed 3d topography measurement based on fringe projection: a review," *Laser & Optoelectronics Progress*, vol. 60, no. 8, p. 0811001, 2023.
- [7] V. Srinivasan, H.-C. Liu, and M. Halioua, "Automated phase-measuring profilometry of 3-d diffuse objects," *Applied optics*, vol. 23, no. 18, pp. 3105–3108, 1984.
- [8] G. Sansoni, S. Corini, S. Lazzari, R. Rodella, and F. Docchio, "Three-dimensional imaging based on gray-code light projection: characterization of the measuring algorithm and development of a measuring system for industrial applications," *Applied Optics*, vol. 36, no. 19, pp. 4463–4472, 1997.
- [9] C. Zuo, S. Feng, L. Huang, T. Tao, W. Yin, and Q. Chen, "Phase shifting algorithms for fringe projection profilometry: A review," *Optics and lasers in engineering*, vol. 109, pp. 23–59, 2018.
- [10] Y. Wang, K. Liu, Q. Hao, X. Wang, D. L. Lau, and L. G. Hassebrook, "Robust active stereo vision using kullback-leibler divergence," *IEEE transactions on pattern analysis and machine intelligence*, vol. 34, no. 3, pp. 548–563, 2012.
- [11] M. Gupta, Q. Yin, and S. K. Nayar, "Structured light in sunlight," in *Proceedings of the IEEE International Conference on Computer Vision (ICCV)*, pp. 545–552, 2013.
- [12] M. Gupta and N. Nakhate, "A geometric perspective on structured light coding," in *Proceedings of the European Conference on Computer Vision (ECCV)*, pp. 87–102, 2018.

- [13] Y. Zhang, D. L. Lau, and Y. Yu, "Causes and corrections for bimodal multi-path scanning with structured light," in *Proceedings of IEEE Conference on Computer Vision and Pattern Recognition (CVPR)*, pp. 4431–4439, 2019.
- [14] Y. Zhang, D. Lau, and D. Wipf, "Sparse multi-path corrections in fringe projection profilometry," in *Proceedings of IEEE Conference on Computer Vision and Pattern Recognition (CVPR)*, pp. 13344–13353, 2021.
- [15] Y. Zhang and D. L. Lau, "Bimodalps: Causes and corrections for bimodal multi-path in phase-shifting structured light scanners," *IEEE Transactions on Pattern Analysis and Machine Intelligence*, 2022.
- [16] S. K. Nayar and M. Gupta, "Diffuse structured light," in *Proceedings of IEEE International Conference on Computational Photography (ICCP)*, pp. 1–11, IEEE, 2012.
- [17] L. Lu, C. Bu, Z. Su, B. Guan, Q. Yu, W. Pan, and Q. Zhang, "Generative deep-learning-embedded asynchronous structured light for three-dimensional imaging," *Advanced Photonics*, vol. 6, no. 4, pp. 046004–046004, 2024.
- [18] M. Gupta, Y. Tian, S. G. Narasimhan, and L. Zhang, "A combined theory of defocused illumination and global light transport," *International Journal of Computer Vision*, vol. 98, pp. 146–167, 2012.
- [19] S. Achar and S. G. Narasimhan, "Multi focus structured light for recovering scene shape and global illumination," in *Proceedings of the European Conference on Computer Vision (ECCV)*, pp. 205–219, Springer, 2014.
- [20] V. Couture, N. Martin, and S. Roy, "Unstructured light scanning robust to indirect illumination and depth discontinuities," *International Journal of Computer Vision*, vol. 108, pp. 204–221, 2014.
- [21] H. Jiang, Y. Li, H. Zhao, X. Li, and Y. Xu, "Parallel single-pixel imaging: A general method for direct-global separation and 3d shape reconstruction under strong global illumination," *International Journal of Computer Vision*, vol. 129, pp. 1060–1086, 2021.
- [22] Y. Zhang, Z. Xiong, Z. Yang, and F. Wu, "Real-time scalable depth sensing with hybrid structured light illumination," *IEEE Transactions on Image Processing*, vol. 23, no. 1, pp. 97–109, 2013.
- [23] C. Zuo, Q. Chen, G. Gu, S. Feng, F. Feng, R. Li, and G. Shen, "High-speed three-dimensional shape measurement for dynamic scenes using bi-frequency tripolar pulse-width-modulation fringe projection," *Optics and Lasers in Engineering*, vol. 51, no. 8, pp. 953–960, 2013.
- [24] S. Zhu, Z. Wu, J. Zhang, Q. Zhang, and Y. Wang, "Superfast and large-depth-range sinusoidal fringe generation for multi-dimensional information sensing," *Photonics Research*, vol. 10, no. 11, pp. 2590–2598, 2022.
- [25] Y. Wang and S. Zhang, "Superfast multifrequency phase-shifting technique with optimal pulse width modulation," *Optics Express*, vol. 19, no. 6, pp. 5149–5155, 2011.
- [26] M. Gupta and S. K. Nayar, "Micro phase shifting," in *Proceedings of IEEE Conference on Computer Vision and Pattern Recognition (CVPR)*, pp. 813–820, IEEE, 2012.
- [27] K. Zhong, Z. Li, Y. Shi, C. Wang, and Y. Lei, "Fast phase measurement profilometry for arbitrary shape objects without phase unwrapping," *Optics and Lasers in Engineering*, vol. 51, no. 11, pp. 1213–1222, 2013.
- [28] Z. Wu, C. Zuo, W. Guo, T. Tao, and Q. Zhang, "High-speed three-dimensional shape measurement based on cyclic complementary gray-code light," *Optics Express*, vol. 27, no. 2, pp. 1283–1297, 2019.
- [29] Z. Wu, W. Guo, and Q. Zhang, "High-speed three-dimensional shape measurement based on shifting gray-code light," *Optics Express*, vol. 27, no. 16, pp. 22631–22644, 2019.
- [30] Z. Wu, W. Guo, Y. Li, Y. Liu, and Q. Zhang, "High-speed and high-efficiency three-dimensional shape measurement based on gray-coded light," *Photonics Research*, vol. 8, no. 6, pp. 819–829, 2020.
- [31] S. Feng, Q. Chen, G. Gu, T. Tao, L. Zhang, Y. Hu, W. Yin, and C. Zuo, "Fringe pattern analysis using deep learning," *Advanced photonics*, vol. 1, no. 2, pp. 025001–025001, 2019.
- [32] J. Song, K. Liu, A. Sowmya, and C. Sun, "Super-resolution phase retrieval network for single-pattern structured light 3d imaging," *IEEE Transactions on Image Processing*, vol. 32, pp. 537–549, 2022.
- [33] T. Weise, B. Leibe, and L. Van Gool, "Fast 3d scanning with automatic motion compensation," in *Proceedings of IEEE Conference on Computer Vision and Pattern Recognition (CVPR)*, pp. 1–8, IEEE, 2007.
- [34] Z. Liu, P. C. Zibley, and S. Zhang, "Motion-induced error compensation for phase shifting profilometry," *Optics Express*, vol. 26, no. 10, pp. 12632–12637, 2018.
- [35] J. Qian, T. Tao, S. Feng, Q. Chen, and C. Zuo, "Motion-artifact-free dynamic 3d shape measurement with hybrid fourier-transform phase-shifting profilometry," *Optics Express*, vol. 27, no. 3, pp. 2713–2731, 2019.
- [36] X. Liu, T. Tao, Y. Wan, and J. Kofman, "Real-time motion-induced-error compensation in 3d surface-shape measurement," *Optics Express*, vol. 27, no. 18, pp. 25265–25279, 2019.
- [37] Y. Wang, V. Suresh, and B. Li, "Motion-induced error reduction for binary defocusing profilometry via additional temporal sampling," *Optics Express*, vol. 27, no. 17, pp. 23948–23958, 2019.
- [38] L. Lu, J. Xi, Y. Yu, and Q. Guo, "New approach to improve the accuracy of 3-d shape measurement of moving object using phase shifting profilometry," *Optics Express*, vol. 21, no. 25, pp. 30610–30622, 2013.
- [39] L. Lu, Y. Yin, Z. Su, X. Ren, Y. Luan, and J. Xi, "General model for phase shifting profilometry with an object in motion," *Applied Optics*, vol. 57, no. 36, pp. 10364–10369, 2018.
- [40] L. Lu, Y. Ding, Y. Luan, Y. Yin, Q. Liu, and J. Xi, "Automated approach for the surface profile measurement of moving objects based on psp," *Optics Express*, vol. 25, no. 25, pp. 32120–32131, 2017.
- [41] Y. Wang, Z. Liu, C. Jiang, and S. Zhang, "Motion induced phase error reduction using a hilbert transform," *Optics Express*, vol. 26, no. 26, pp. 34224–34235, 2018.
- [42] G. Wu, T. Yang, F. Liu, and K. Qian, "Suppressing motion-induced phase error by using equal-step phase-shifting algorithms in fringe projection profilometry," *Optics Express*, vol. 30, no. 11, pp. 17980–17998, 2022.
- [43] W. Guo, Z. Wu, Q. Zhang, and Y. Wang, "Real-time motion-induced error compensation for 4-step phase-shifting profilometry," *Optics Express*, vol. 29, no. 15, pp. 23822–23834, 2021.
- [44] T. F. Lam, H. Blum, R. Siegwart, and A. Gawel, "SI sensor: An open-source, real-time and robot operating system-based structured light sensor for high accuracy construction robotic applications," *Automation in Construction*, vol. 142, p. 104424, 2022.
- [45] G. Zhang, C. Zhu, and K. Liu, "Binomial self-compensation for motion error in dynamic 3d scanning," in *Proceedings of the European Conference on Computer Vision (ECCV)*, Springer, 2024.
- [46] J. Baqersad, P. Poozesh, C. Niezrecki, and P. Avitabile, "Photogrammetry and optical methods in structural dynamics—a review," *Mechanical Systems and Signal Processing*, vol. 86, pp. 17–34, 2017.
- [47] J. Carr, J. Baqersad, C. Niezrecki, and P. Avitabile, "Full-field dynamic strain on wind turbine blade using digital image correlation techniques and limited sets of measured data from photogrammetric targets," *Experimental Techniques*, vol. 40, pp. 819–831, 2016.
- [48] C. Zuo, T. Tao, S. Feng, L. Huang, A. Asundi, and Q. Chen, "Micro fourier transform profilometry (μ ftp): 3d shape measurement at 10,000 frames per second," *Optics and Lasers in Engineering*, vol. 102, pp. 70–91, 2018.
- [49] Y. Wang and S. Zhang, "Optimal pulse width modulation for sinusoidal fringe generation with projector defocusing," *Optics Letters*, vol. 35, no. 24, pp. 4121–4123, 2010.
- [50] Z. Li, K. Zhong, Y. F. Li, X. Zhou, and Y. Shi, "Multiview phase shifting: a full-resolution and high-speed 3d measurement framework for arbitrary shape dynamic objects," *Optics Letters*, vol. 38, no. 9, pp. 1389–1391, 2013.
- [51] T. Tao, Q. Chen, S. Feng, J. Qian, Y. Hu, L. Huang, and C. Zuo, "High-speed real-time 3d shape measurement based on adaptive depth constraint," *Optics Express*, vol. 26, no. 17, pp. 22440–22456, 2018.
- [52] J. Qian, S. Feng, T. Tao, Y. Hu, Y. Li, Q. Chen, and C. Zuo, "Deep-learning-enabled geometric constraints and phase unwrapping for single-shot absolute 3d shape measurement," *APL Photonics*, vol. 5, no. 4, 2020.
- [53] W. Yin, S. Feng, T. Tao, L. Huang, M. Trusiak, Q. Chen, and C. Zuo, "High-speed 3d shape measurement using the optimized composite fringe patterns and stereo-assisted structured light system," *Optics Express*, vol. 27, no. 3, pp. 2411–2431, 2019.
- [54] Y. Zhang, Z. Xiong, and F. Wu, "Unambiguous 3d measurement from speckle-embedded fringe," *Applied Optics*, vol. 52, no. 32, pp. 7797–7805, 2013.
- [55] B. Jähne, "Release 4 of the emva 1288 standard: Adaption and extension to modern image sensors," in *Forum Bildverarbeitung 2020*, pp. 13–24, KIT Scientific Publishing Karlsruhe, Germany, 2020.
- [56] L. Shenzhen and Q. Kemao, "Modeling the measurement precision of fringe projection profilometry," *Light: Science & Applications*, vol. 12, no. 1, p. 257, 2023.
- [57] H. O. Saldner and J. M. Huntley, "Temporal phase unwrapping: application to surface profiling of discontinuous objects," *Applied optics*, vol. 36, no. 13, pp. 2770–2775, 1997.
- [58] Y. Ding, J. Xi, Y. Yu, and J. Chicharo, "Recovering the absolute phase maps of two fringe patterns with selected frequencies," *Optics letters*, vol. 36, no. 13, pp. 2518–2520, 2011.



Geyou Zhang received the B.E. and M.E. degrees from the College of Electrical Engineering at Sichuan University in 2020 and 2023, respectively. He is currently pursuing a Ph.D. in the School of Information and Communication Engineering at the University of Electronic Science and Technology of China. His research interests include 3D imaging, with a focus on structured light illumination, stereo vision, and dynamic 3D scanning.



Kai Liu received the BS and MS degrees in computer science from Sichuan University, China in 1996 and 2001, and the PhD degree in electrical engineering from the University of Kentucky in 2010, respectively. He is currently a professor in the College of Electrical Engineering at Sichuan University. He was a postdoctoral researcher in the Information Access Lab at the University of Delaware from September 2010 to July 2011. His main research interests include computer/machine vision, active/passive stereo vision, and image processing.

processing.



Ce Zhu (M'03–SM'04–F'17) received the B.S. degree from Sichuan University, Chengdu, China, in 1989, and the M.Eng and Ph.D. degrees from Southeast University, Nanjing, China, in 1992 and 1994, respectively, all in electronic and information engineering. He held a post-doctoral research position with the Chinese University of Hong Kong in 1995, the City University of Hong Kong, and the University of Melbourne, Australia, from 1996 to 1998. He was with Nanyang Technological University, Singapore, for 14 years from 1998 to 2012,

where he was a Research Fellow, a Program Manager, an Assistant Professor, and then promoted to an Associate Professor in 2005. He has been with University of Electronic Science and Technology of China, China, as a Professor since 2012. His research interests include video coding and communications, video analysis and processing, 3D video, visual perception and applications.

He has served on the editorial boards of a few journals, including as an Associate Editor of IEEE TIP, IEEE TCSVT, IEEE T BROADCAST, IEEE SPL, an Editor of IEEE COMMUN SURV TUT, and an Area Editor of SPIC. He has also served as a Guest Editor of a few special issues in international journals, including as a Guest Editor in the IEEE J-STSP. He is an APSIPA Distinguished Lecturer (2021-2022), and was also an IEEE Distinguished Lecturer of Circuits and Systems Society (2019-2020). He is a co-recipient of multiple paper awards at international conferences, including the most recent Best Demo Award in IEEE MMSP 2022, and the Best Paper Runner-Up Award in IEEE ICME 2020.